Microbial engineering of nano-heterostructures; biological synthesis of a magnetically-recoverable palladium nanocatalyst

Victoria S Coker[1*], James A Bennett[2], Neil Telling[1], Torsten Henkel[1], John M Charnock[1], Gerrit van der Laan[3,1], Richard AD Pattrick[1], Carolyn I Pearce[1], Richard S Cutting[1], Ian J Shannon[2], Joe Wood[4], Elke Arenholz[5], Ian C. Lyon[1] & Jonathan R. Lloyd[1]

[1]*School of Earth, Atmospheric & Environmental Sciences and Williamson Research Centre for Molecular Environmental Science, University of Manchester, Manchester M13 9PL, UK*

[2]*School of Chemistry, University of Birmingham, Birmingham B15 2TT, UK*

[3]*Diamond Light Source Ltd, Didcot, Oxfordshire, OX11 0DE, UK*

[4]*School of Chemical Engineering, University of Birmingham, Birmingham B15 2TT, UK*

[5]*Advanced Light Source, Lawrence Berkeley National Laboratory, Berkeley, CA 94720, USA*

*vicky.coker@manchester.ac.uk

Abstract

Precious metals supported on ferrimagnetic particles form a diverse range of catalysts. Here we show a novel biotechnological route for the synthesis of a heterogeneous catalyst consisting of reactive palladium nanoparticles arrayed on a biomagnetite support. The magnetic support was synthesised at ambient temperature by the Fe(III)-reducing bacterium, *Geobacter sulfurreducens*, and facilitated ease of

recovery of the catalyst with superior performance due to reduced agglomeration. Arrays of palladium nanoparticles were deposited on the nanomagnetite using a simple one-step method without the need to modify the biomineral surface most likely due to an organic coating priming the surface for Pd adsorption. A combination of EXAFS and XPS showed the particles to be predominantly metallic in nature. The Pd^0-biomagnetite was tested for catalytic activity in the Heck Reaction coupling iodobenzene to ethyl acrylate or styrene and near complete conversion to ethyl cinnamate or stilbene was achieved within 90 and 180 min, respectively.

Introduction

Nanoparticles make highly desirable catalysts, often offering unique properties linked to their very high surface area. Palladium, placed on a suitable support material makes an exceptional catalyst well known for mild reaction conditions and exhibiting excellent compatibility with many polar functional groups and a high degree of chemo-, regio- and even stereoselectivity [1]. Magnetic nanoparticles are particularly useful support materials for catalysts as they can combine the advantages of high dispersion through a liquid with ease of recovery [2,3]. Thus, coating magnetic nanoparticles with precious metals such as palladium results in a highly functional catalyst [4-7]. Conventional chemical approaches to make these materials have achieved varying degrees of success, as loss of precious metal during recycling can be a problem, and complicated protocols are often employed to functionalise the support material surface [3,4,6,8-10].

Building on earlier work [11], recent studies have revealed biosynthetic routes can be harnessed to make nanoparticles of magnetite (Fe_3O_4) efficiently and at low cost with control over the magnetic properties by substitution of transition metals other than iron into the spinel ferrite structure [12-14]. Two routes are possible for the biological synthesis of nanoscale magnetite. In the first, magnetotactic bacteria synthesise intracellular crystals of single domain magnetite. These are used by the bacteria to orientate the cell within the Earth's magnetic field, helping the organism to guide itself to the sediment-water interface, its preferred ecological niche [15,16]. However, for this route growth yields and indeed, final yields of intracellular magnetite are very low. In the second route, dissimilatory Fe(III)-reducing bacteria such as *Geobacter* species can produce copious quantities of extracellular nanoscale magnetite through the respiration of poorly crystalline Fe(III) oxides and oxyhydroxides [11]. These specialist anaerobic bacteria live in environments depleted of oxygen and therefore conserve energy for growth by transferring electrons from the oxidation of simple carbon sources, such as acetate, to Fe(III) or Mn(IV)-bearing minerals [17]. This mechanism of nano-magnetite formation involves the extracellular reduction of Fe(III)-oxyhydroxides causing the release of soluble Fe(II), resulting in complete recrystallisation of the amorphous mineral into the new, relatively reduced, highly crystalline magnetic phase [18,19]. Especially relevant to manufacturing, these enzyme-driven reactions take place on the scale of hours, at ambient pressures and temperatures and use inexpensive feedstocks [18]. Thus, nanoscale biomagnetite is a potential support material for industrial catalysts, especially if simplified protocols for functionalising the bionanomineral surface can be developed.

Here we describe the bio-production of such a catalyst comprising of biomagnetite functionalised with palladium nanoparticles and involving a minimal level of downstream processing. The effectiveness of this catalyst is demonstrated for the Heck coupling of iodobenzene with styrene or ethyl acrylate. Heck chemistry is of wide-ranging industrial importance, providinga single step route to the arylation, alkylation or vinylation of various alkenes [20,21]. Traditionally a palladium-phosphine catalyst is used, although a large amount of literature is devoted to the study of a variety of different catalysts for these reactions [20,22]. This work opens the door to the development of an energy efficient, environmentally friendly route to manufacture novel magnetic heterostructures which can be employed in a wide range of applications.

Main text

A biogenic nanoscale magnetite support was first produced by anoxic washed cell suspensions of *Geobacter sulfurreducens* challenged with Fe(III)-oxyhydroxide, an electron donor (sodium acetate) and a redox mediator [9,10-anthraquinone-2,6-disulphonate (AQDS)]. After approximately 8 h, the Fe(III)-oxyhydroxide had been completely converted to magnetite. Production of the functionalised Pd-coated magnetite was concluded through the addition of a solution of $NaPdCl_4$ to the water-washed nano-magnetite suspension under an anoxic atmosphere (N_2:H_2 = 97%:3%); optimisation studies revealed that removal of soluble palladium occurred rapidly, within an hour, and was efficient over a range of Pd(II) concentrations up to 10 mol% Pd.

Detailed examination was undertaken of a nano-magnetite functionalised with a ~5 mol% Pd loading, produced by mixing the Pd(II) solution and biomagnetite for 12 h prior to washing in deionised water. Transmission electron microscope (TEM) images of the material produced before (Fig 1a) and after (Fig 1b) precipitation of Pd onto the surface of biomagnetite are shown. Fig. 1(a) shows the magnetite to have a consistent particle size range of 20 nm to 30 nm. However, after addition of Pd, two sizes of particle became clearly visible; the high-resolution inset in Fig. 1b shows how smaller particles (~5 nm) are attached to the larger particles (~20 nm). Energy dispersive X-ray (EDX) analysis using a relatively unfocussed beam showed the bulk sample (Fig 1b) to contain ~3.5 at% Pd. Using an EDX spot size of 5-6 nm, analyses (Fig 1b inset, point 1) indicated that the larger particles contained less than 1 at% Pd whereas analyses centred on the smaller particles (Fig 1b inset, point 2) suggested that they were enriched for the precious metal (9-10 at% Pd). These results indicate that the larger particles are the biomagnetite crystals decorated with small Pd particles. Both small and large particles displayed continuous lattice fringes, indicative of well-crystalline single crystals. TEM selected area electron diffraction (SAED) analysis (Fig. 1c) of the particles with supporting data from powder X-ray diffraction (PXRD) (Fig. 1d) confirmed that the material contained Bragg reflections consistent with the presence of magnetite with less pronounced reflections consistent with Pd metal; the latter are broader than those for magnetite owing to their smaller particle size. Crystallite size was estimated by applying the Scherrer equation to the (311) peak of magnetite in Fig. 1(d) which resulted in a mean crystallite size of 27.2 nm consistent with the size estimate from electron microscopy imaging. In addition, although much weaker it was possible to obtain an estimate of the Pd crystallite

size from the Pd (311) peak which gave a value of ~5 nm, again in good agreement with TEM images.

In most examples of supported Pd catalyst manufacture, an organic ligand or silica shell is used to aid attachment of the Pd to the support [4,5] for example 3-aminopropyl triethoxysilane (APTS)[5]. However, in the case of biogenic magnetite no pre-coating with a ligand was required to aid attachment of Pd. Thus, to characterise the surface of biogenic magnetite, samples prior to Pd(II) addition were analysed using Time-of-Flight Secondary Ion Mass Spectrometry (TOF-SIMS), as this technique is very sensitive to both organic and inorganic compounds. Images of different secondary ions (SI) associated with either Fe, Al or organic material on the surface of a washed biogenic nanomagnetite (Fig. 2(a)) were compared to the maps from a synthetically produced nanomagnetite (Alfa Aesar, Heysham, UK) (Fig. 2(b)). Fig. 2 illustrates that there is a significant quantity of organic material associated with the biogenic magnetite, as the representative secondary ion images of organic molecules spatially correlate with the Fe map, whereas the inorganic magnetite showed no significant organic signature corresponding to the spatial distribution of Fe. Depth profiling of the organic layer using C_{60} primary ions (PI) indicated that the organic layer is indeed a coating on the nanomagnetite. One bombardment of ~10^{15}PI/cm^2 resulted in a decrease of the SI-signals associated with the organic material by a factor of approximately 100 (Fig 2(c)) whereas the SI-signals associated with the nanomagnetite stayed almost constant. Some of the secondary ion ratios for the Fe-bearing clusters in Fig 2(c) are below a value of one, as ionisation efficiencies change slightly with decreasing amounts of organic material. The

presence of an organic coating explains the ability of the nanomagnetite to adsorb Pd without the need to pre-coat the washed nanoparticles prior to introducing the Pd solution. A likely source of the organic material is extracellular polymeric substance (EPS), a common product of bacterial pure cultures and communities, as this has previously been found bound to biogenic uranium nanoparticulate material[23]. We are not, however, excluding the presence of other cell exudates or constituents released after lysis of dead cells.

Using X-ray absorption (XA) spectroscopy, the Fe *K*-edge absorption spectra of biomagnetite before and after the addition of Pd were collected to provide the extended X-ray absorption fine structure (EXAFS) [Fig. 3a (i, ii); Table 1] and their corresponding Fourier transform [Fig. 3b (i, ii); Table 1]. The EXAFS data provided an excellent fit for a magnetite structure for both samples, with the bond lengths for the tetrahedral (T_d) and octahedral (O_h) sites showing slight shortening after addition of Pd from 1.85 to 1.80 Å and from 2.03 to 2.00 Å, respectively. Incorporating Pd atoms did not improve the fit, indicating that the nanoparticulate Pd attached directly to the iron cations in magnetite or via bridging oxygens was below the limit of detection. XA was additionally used to obtain the Fe $L_{2,3}$-edge within a magnetic field and thus provide the X-ray magnetic circular dichroism (XMCD) difference spectra of these samples (Fig. 4a). The Fe $L_{2,3}$-edge XMCD can distinguish between the three Fe cation environments present in ferrite spinel structures to a depth of ~65 Å as the intensities of the peaks labelled in Fig. 3a(i) relate to the amount of Fe^{2+} O_h (octahedral), Fe^{3+} T_d (tetrahedral), and Fe^{3+} O_h respectively (see [24-26] for details). Fig. 4a(i) displays the Fe $L_{2,3}$-edge XMCD spectrum for biomagnetite without addition of Pd that after fitting gave an Fe^{2+}/Fe^{3+} ratio of 0.64,

161 indicating an excess of Fe^{2+} compared to a typical stoichiometric magnetite which would
162 have a ratio of 0.50, consistent with previous results for biogenic magnetites [27,28]. The
163 addition of Pd resulted in an increase in the amount of Fe^{2+}, forming a spinel with a
164 Fe^{2+}/Fe^{3+} ratio of 0.70 (Fig. 3b). The reduction of Fe^{3+} to Fe^{2+} in the spinel relates, most
165 likely, to the ability of Pd^0 nanoparticles to absorb large quantities of hydrogen which
166 then interacts with the outer Fe atoms causing reduction to Fe^{2+}.
167
168 EXAFS and X-ray photoelectron spectroscopy (XPS) were used to determine the
169 nature of the Pd particles deposited on the surface of the magnetite. EXAFS and the
170 related fourier transform from the Pd *K*-edge [Fig. 3(a,b)(iv)] for Pd-biomagnetite could
171 be fitted with 5 coordination shells of atoms the first shell containing 12 Pd scatterers in
172 at 2.74 Å and the second shell 6 Pd scatterers at 3.84 Å (see Table 1); these data have an
173 excellent correspondence to values for Pd metal foil [Fig. 3(a,b)(iii)]. Fitting the Pd 3*d*
174 XPS spectrum (Fig. 4b) indicated that the main Pd peak had a binding energy of 335.3 eV
175 with a minor peak (6% intensity) at a binding energy of 336.8 eV. These compare well
176 with literature values that show the main peak to be Pd^0 [29] and the weak peak to be a
177 second phase that may be PdO or PdO_2 [30]. Pd-oxide could be present due to either
178 oxidation of the surface of the metallic Pd or the Pd nanoparticles could be attaching to
179 the magnetite via 'bridging' oxygens. Additional XPS data (not shown) indicated that the
180 surface of the nanoparticles had an Fe:Pd ratio of 1.00:0.22. Thus the TEM, XAS and
181 XPS data are consistent and confirm the presence of Pd^0 nanoparticles attached to a
182 biomagnetite support. Samples were kept under anoxic conditions throughout the

183 preparation and measurement when using the surface sensitive techniques XMCD and
184 XPS to ensure that the samples were not air oxidised.
185
186 The definitive test of the usefulness of the 5 mol% Pd-coated biomagnetite is its
187 catalytic potential and therefore Heck Reaction coupling of iodobenzene to styrene or
188 ethyl acrylate was performed. Identical catalytic testing was also carried out on colloid
189 stabilised nanoparticulate palladium[31-33] as a means of comparing the Pd-coated
190 biomagnetite to a highly active conventional catalyst. The Pd-coated biomagnetite was
191 found to be active in the coupling of both olefins, with the complete conversion of the
192 iodobenzene (plus ethyl acrylate or styrene) to ethyl cinnamate or stilbene within 90 and
193 180 min, respectively. Rates of reaction were equal or superior to those obtained with an
194 equimolar amount of Pd from the colloidal palladium catalyst. However, the advantage of
195 the magnetite-based catalyst was that it could be readily recovered at the end of the
196 reaction by simply decanting the solution from the reaction vessel while retaining the
197 solid catalyst by applying a magnetic field to the base of the flask. The solid was washed
198 and dried before use in subsequent reactions.
199
200 Successive runs were performed for the Heck coupling of iodobenzene and ethyl
201 acrylate to test the Pd-coated magnetite for recyclability. Although a small decrease in
202 initial reaction rate was observed in each successive cycle, virtually quantitative
203 conversions were reached in 120 min for each run, up to a fourth cycle (Fig. 5), an
204 improvement on some literature values for conventional catalysts [5]. These experiments
205 were conducted without attempting to exclude air and the decrease in activity is attributed

206 to the loss of a small amount of material due to oxidation of some of the magnetite
207 support to a non-magnetic phase material which was not recovered between runs, rather
208 than direct loss of Pd to solution. Indeed, ICP-AES analysis of the supernatant in each
209 cycle confirmed that there was negligible loss of Pd or indeed Fe to solution (data not
210 shown). By comparison although the palladium colloids remained catalytically active for
211 a second cycle of the ethyl acrylate coupling the halide conversion was only 89 %
212 compared to > 99% for Pd-coated biomagnetite (Fig. 5). In addition more than 75% of
213 the mass of the catalyst was lost during the recovery step, most likely due to the tertiary
214 butyl ammonium bromide capping layer dissolving in the solvent. This would lead to the
215 remaining palladium aggregating, reducing the active surface area substantially. Further
216 recycling after the second run was unfeasible due to the very low mass of remaining
217 material.
218
219 These results demonstrate that a novel biomagnetite-supported Pd-nanoparticle
220 catalyst has several major advantages over conventional colloidal Pd catalysts. First,
221 recovery and recycling is facile and, second, the biomagnetite support keeps the Pd
222 dispersed and prevents it from agglomerating and losing vital surface area. The
223 preparation method, apart from its novelty, provides an organics-coated ferrite particle in
224 a one-step process, allowing Pd nanoparticles to be attached to the support material
225 without further processing. Bacterial production is a low cost environmentally-friendly
226 biotechnological route of manufacture, which opens up a route to the manufacture of
227 other precious metal nanocatalysts. Recent success at applying gold and platinum derived
228 materials to biogenic magnetite as supported nanoparticles (unpublished data) indicates

229 the versatility of bacterial production of nanocatalysts, which could be applied to a wide
230 range of catalytic reactions.
231
232
233 **Methods**
234 As previously described, magnetite production was achieved by the reduction of
235 Fe(III)-oxyhydroxide in the presence of AQDS using *G. sulfurreducens* [13] , under an
236 atmosphere of N_2–CO_2 (80:20). Bottles were incubated in the dark at 30°C for two days
237 after which magnetite had been produced. The resulting magnetite was washed twice in
238 degassed deionised water and then re-suspended in water using its magnetic properties to
239 separate the mineral from the supernatant. An aliquot of a solution of sodium
240 tetrachloropalladate (Na_2PdCl_4, Sigma-Aldrich CAS no. 13820-53-6) was then added so
241 that the final concentration of Pd was 5% by mass of the magnetite. The magnetite
242 suspension was left overnight in a shaking incubator at 150 rpm and 20°C. The sample
243 was then washed again twice using degassed, distilled deionised water twice before
244 drying under anoxic conditions.
245
246 The Time-of-Flight Secondary Ion Mass Spectrometry (TOF-SIMS) analyses
247 were carried out using the IDLE instrument[34] which was equipped with a C_{60} primary ion
248 gun[35]. Chemical damage by C_{60} primary ions is far less than by any other primary ion
249 species so that depth profiling of organic samples becomes feasible[36]. Analysis of
250 inorganic material is also improved[37] enabling comprehensive investigation of mixed
251 samples. Only a few atomic layers are sputtered during each measurement making TOF-

252 SIMS an ideal method to study thin layers on sample surfaces with sensitivities high
253 enough to analyze trace element abundances. As the beam is rastered over the measured
254 area a complete mass spectrum is recorded at each point allowing for comprehensive
255 offline analysis. Secondary ion distribution images have been reconstructed for all
256 interesting mass intervals and background-corrected count integrals for all these mass
257 intervals have been used for quantitative analysis. The magnetite samples have been
258 mounted on Al stubs in a thick layer of around one hundred micro-metres and analyses
259 have been carried out with a lateral resolution of 2μm and a field-of-view of
260 $480\times365\mu m^2$.
261
262 X-ray absorption (XA) spectra were collected for the Fe and Pd *K* edges on
263 beamline 9.3 at the Synchrotron Radiation Source (SRS), Daresbury Laboratory. A
264 double crystal Si(311) monochromator was used, detuned to 70% transmission for
265 harmonic rejection. Pd *K*-edges were collected at 80 K in fluorescence mode using a 9-
266 element Ge detector. Fe *K*-edges and a standard palladium foil were collected at 80 K in
267 transmission mode. Background subtracted EXAFS spectra were analyzed in EXCURV98
268 using full-curved-wave theory as described in Henderson et al. (2007)[38], which allows the
269 proportion of metal in each site to be refined as a single parameter. The metallic-phase Pd
270 K-edge spectra were analysed in EXCURV98 using a model based on the crystal
271 structure of Pd[39] the Fermi energy correction and the absorber-scatterer distances and
272 Debye-Waller factors were refined to minimise a least squares residual.
273

XA spectra for XMCD were collected on beamline 4.0.2 at the Advanced Light Source (ALS), Berkeley, CA, using the octopole magnet endstation [40]. Powders were mounted on carbon tape attached to the sample manipulator and kept in O_2-free conditions throughout. XA was monitored in total-electron yield mode, which gives an effective probing depth of ~4.5 nm. At each energy point the XA was measured for the two opposite magnetisation directions by reversing the applied field of 0.6 T. The XA spectra of the two magnetisation directions were normalised to the incident beam intensity and subtracted from each other to give the XMCD spectrum [24]. Spectra were fitted by means of a non-linear least-squares analysis, using calculations for each of the Fe sites [24]. In these calculations, as described elsewhere [41], the Hartree-Fock Slater integrals for the 3*d*-3*d* and 2*p*-3*d* Coulomb and exchange interactions were scaled to 70% and 80%, respectively, and the crystal fields for the O_h and T_d sites were taken to be $10Dq$ = 1.2 eV and -0.6 eV, respectively. The calculated spectra were convoluted by a Lorentzian of Γ= 0.3 (0.5) eV for the L_3 (L_2) edge to account for intrinsic core-hole lifetime broadening and by a Gaussian of σ = 0.15 eV to account for instrumental broadening.

TEM was conducted using a Phillips/FEI CM200 equipped with a field emission Gun, EDX system (Oxford Instruments UTW ISIS) and a Gatan imaging filter. All TEM images presented here are bright-field images obtained using an operating beam voltage of 200 keV. Selected area electron diffraction (SAED) patterns were acquired using an appropriate diffraction aperture. A droplet of washed sample was placed on a carbon grid (Agar Scientific) and allowed to dry before imaging.

X-ray photoelectron spectroscopy (XPS) data were recorded using a Kratos Axis Ultra employing a monochromated Al *K*α X-ray source and an analyser pass energy of 20eV, resulting in a total energy resolution of ~0.9eV. Uniform charge neutralisation of the photoemitting surface was achieved by exposing the surface to low energy electrons in a magnetic immersion lens system (Kratos Ltd.). The system base pressure was 5×10^{-10} mbar. All samples were dried anaerobically and the resulting powders were loaded into the spectrometer via a dry nitrogen glove box to avoid exposure to atmospheric oxygen. Photoelectron binding energies (BE) were referenced to C1*s* adventitious carbon contamination peaks set at 285eV BE. The electron energy analyser was calibrated using elemental references: Au4$f_{7/2}$ (83.98eV BE), Ag3$d_{5/2}$ (368.26eV BE) and Cu2$p_{3/2}$ (932.67eV BE). An appropriate (Shirley) background was removed from all spectra [42].

To test the catalytic properties of the Pd-coated biomagnetite dry DMF (15 mL), 5% wt Pd magnetite catalyst (10.6 mg, 0.5 mol %), iodobenzene (204 mg, 1 mmol) and trienthylamine (0.21 mL, 1.5 mmol) were added to a 2-necked round bottomed flask, equipped with reflux condenser under a nitrogen atmosphere, and the mixture heated to 120 ^{o}C with stirring. Olefin substrate (1.5 mmol) was added and the mixture stirred at 120 ^{o}C under nitrogen. Samples were taken from the reaction periodically for analysis by high performance liquid chromatography using a Dionex Summit HPLC (with Chromeleon software) with a Summit p580 quaternary low pressure gradient pump, Summit UVD 170s UV/VIS multichannel detector with analytical flow cell and a Phenomenex Luna 10u C18 (2) Column, 250 mm x 4.6 id. A flow rate of 1 ml/min was used with a solvent

gradient of 100 % water to 100 % MeCN over 40 min, hold for 10 min, and then back to 100 % water for 10 min. At the end of the reaction, the mixture was allowed to cool to room temperature before decanting the solution from the flask whilst retaining the catalyst by applying a magnetic field to outside of the flask. The solid was washed (5 mL DMF followed by 5 mL acetone) and the solid dried for use in the next run.

Acknowledgements

This work was supported by the EPSRC grants EP/D057310/1 & EP/D058767/1 and BBSRC grant BB/E003788/1. We would like to thank P Wincott for XPS analysis, M Ward for TEM support and J Waters for XRD support. We thank the STFC, Daresbury for beamtime and S Fiddy for assistance with EXAFS. The Advanced Light Source is supported by the Director, Office of Science, Office of Basic Energy Sciences, of the U.S. Department of Energy under Contract No. DE-AC02-05CH11231 and is thanked for XMCD beamtime.

References

1. D'Souza, D. M. & Muller, T. J. J. Multi-component syntheses of heterocycles by transition-metal catalysis. *Chem Soc Rev* **36**, 1095-1108 (2007).

2. Lu, A.-H., Salabas, E. L. & Schuth, F. Magnetic nanoparticles: synthesis, protection, functionalization and application. *Angewandte Chemie* **46**, 1222-1244 (2007).

3. Baruwati, B., Guin, D. & Manorama, S. V. Pd on surface-modified NiFe2O4 nanoparticles: a magnetically recoverable catalyst for Suzuki and Heck reactions. *Organic Letters* **9**, 5377-5380 (2007).

4. Rossi, L. et al. Superparamagnetic nanoparticle-supported palladium: a highly stable magnetically recoverable and reusable catalyst for hydrogenation reactions. *Green Chemistry* **9**, 379-385 (2007).

5. Wang, Z. L., Shen, B., Aihua, Z. & He, N. Synthesis of Pd/Fe_3O_4 nanoparticle-based catalyst for the cross-coupling of acrylic acid with iodobenzene. *Chemical Engineering Journal* **113**, 27-34 (2005).

6. Wang, Z., Xiao, P., Shen, B. & He, N. Synthesis of palladium-coated magnetic nanoaprticle and its application in Heck reaction. *Colloids and Surfaces A: Physicochem. Eng. Aspects* **276**, 116-121 (2006).

7. Mizukoshi, Y., Sato, K., Konno, T. J., Masahashi, N. & Tanabe, S. Magnetically Retrievable Palladium/Maghemite Nanocomposite Catalysts Prepared by Sonochemical Reduction Method. *Chemistry Letters* **37**, 922-923 (2008).

8. Kinoshita, T., Seino, S., Mizukoshi, Y., Nakagawa, T. & Yamamoto, T. Functionalization of magnetic gold/iron-oxide composite nanoparticles with oligonucleotides and magnetic separation of specific target. *Journal of Magnetism & Magnetic Materials* **311**, 255-258 (2007).

9. Mandal, M. et al. Magnetite nanoparticles with a tunable gold or silver shell. *Journal of Colloidal and Interface Science* **286**, 187-194 (2005).

10. Auer, E., Freund, A., Pietsch, J. & Tacke, T. Carbons as supports for industrial precious metal catalysts. *Applied Catalysis A: General* **173**, 259-271 (1998).

11. Lovley, D. R., Stoltz, J. F., Nord Jr, G. L. & Phillips, E. J. P. Anaerobic production of magnetite by a dissimilatory iron-reducing microorganism. *Nature* **330**, 252-254 (1987).

12. Moon, J.-W. et al. Magnetic response of microbially synthesized transition metal- and lanthanide-substituted nanosized magnetites. *J Magn Magn Mater* **313**, 283-292 (2007).

13. Coker, V. S. et al. Probing the site occupancies of Co, Ni and Mn substituted biogenic magnetite using XAS and XMCD. *Am. Mineral.* **93**, 1119-1132 (2008).

14. Staniland, S. et al. Controlled cobalt doping of magnetosomes *in vivo*. *Nature Nanotechnology* **3**, 158-162 (2008).

15. Blakemore, R. Magnetotactic bacteria. *Science* **190**, 377-379 (1975).

16. Frankel, R. B., Blakemore, R. & Wolfe, R. S. Magnetite in freshwater magnetic bacteria. *Science* **203**, 1355-1357 (1979).

17. Caccavo Jr, F. et al. *Geobacter sulfurreducens* sp. nov., a hydrogen and acetate-oxidising dissimilatory matal reducing. *Appl Environ Microb* **60**, 3752-3759 (1994).

18. Coker, V. S. et al. Time-resolved synchrotron X-ray powder diffraction study of magnetite formation by the Fe(III)-reducing bacterium, *Geobacter sulfurreducens*. *Am Mineral* **93**, 540-547 (2008).

19. Hansel, C. M. et al. Secondary mineralization pathways induced by dissimilatory iron reduction of ferrihydrite under advective flow. *Geochim Cosmochim Ac* **67**, 2977-2992 (2003).

20. Beletskaya, I. P. & Cheprakov, A. V. The Heck Reaction as a Sharpening Stone of Palladium Catalysis. *Chemical Reviews* **100**, 3009-3066 (2000).

21. Polshettiwar, V. & Molnár, Á. Silica-supported Pd catalysts for Heck coupling reactions. *Tetrahedron* **63**, 6949-6976 (2007).

22. Wang, Z., Chen, Z., Gu, J., Li, Y. & Li, W. Occurrence and environmental implications of magnetic iron sulfides in stiff muds from the continental shelf of the East China Sea. *Geo-Marine Lett* **25**, 300-305 (2005).

23. Marshall, M. J. et al. Microorganisms that catalyze changes in oxidation states of metals can be used to decontaminate environments of radionuclides. Here, *c*-type cytochromes on the outer membrane of a dissimilatory metal reducing bacterium are shown to be essential for the reduction of uranium(VI). *PLoS Biol* **4**, e268 (2006).

24. Pattrick, R. A. D. et al. Cation site occupancy in spinel ferrites studied by X-ray magnetic circular dichroism: developing a method for mineralogists. *Eur. J. Mineral.* **14**, 1095-1102 (2002).

25. Pearce, C. I., Henderson, C. M. B., Pattrick, R. A. D., van der Laan, G. & Vaughan, D. J. Direct determination of cation site occupancies in natural ferrite spinels by $L_{2,3}$ x-ray absorption spectroscopy and x-ray magnetic circular dichroism. *American Mineralogist* **91**, 880-893 (2006).

26. Coker, V. S. et al. XAS and XMCD evidence for species-dependent partitioning of arsenic during microbial reduction of ferrihydrite to magnetite. *Environmental Science & Technology* **40**, 7745-7750 (2006).

27. Carvallo, C. et al. Biogenic vs. abiogenic magnetite nanoparticles: A XMCD study. *Am Mineral* **93**, 880-885 (2008).

28. Coker, V. S. et al. Cation site occupancy of biogenic magnetite compared to polygenic ferrite spinels determined by X-ray magnetic circular dichroism. *Eur J Mineral* **19**, 707-716 (2007).

29. Wagner, C. D., Riggs, W. M., Davis, L. E., Moulder, J. F. & Muilenberg, G. E. *Handbook of X-ray Photoelectron Spectroscopy* (Perkin Elmer Corporation, Eden Prairie, Minnesota, 1979).

30. Kim, K. S., Gossmann, A. F. & Winograd, N. X-ray photoelectron spectroscopic studies of palladium oxides and the palladium-oxygen electrode. *Analytical Chemistry* **46**, 197-200 (1974).

31. Bonnemann, H., Brinkmann, R. & Neiteler, P. Preparation and catalytic properties of NR^{+}_{4}-stabilized palladium colloids. *Appl Organometallic Chem* **8**, 361-378 (1994).

32. Reetz, M. T., Breinbauer, R. & Wanninger, K. Suzuki and Heck reactions catalyzed by preformed palladium clusters and palladium/nickel bimetallic clusters. *Tetrahedron Lett* **37**, 4499-4502 (1996).

33. Reetz, M. T. et al. Visualization of surfactants on nanostructured palladium clusters by a combination of STM and high-resolution TEM. *Science* **267**, 367-369 (1995).

34. Henkel, T., Tizard, J., Blagburn, D. & Lyon, I. IDLE - Interstellar Dust Laser Explorer. A new instrument for elemental and isotopic analysis and imaging of interstellar and interplanetary dust. *Review of Scientic Instruments* **78**, 055107 (2007).

35. Hill, R. & Blenkinsopp, P. W. M. The development of C_{60} and gold cluster ion guns for static SIMS analysis. *Applied Surface Science* **231-232**, 936-939 (2004).

36. Fletcher, J. S. et al. TOF-SIMS analysis Using C_{60}. Effect of impact energy on yield and damage. *Analytical Chemistry* **78**, 1827-1831 (2006).

37. Henkel, T., Rost, D. & Lyon, I. C. Improvements in quantification accuracy of inorganic TOFSIMS analysis of silicate materials by using C_{60} primary ions. *Rapid Communications in Mass Spectrometry*, in print (2009).

38. Henderson, C. M. B., Charnock, J. M. & Plant, D. A. Cation occupancies in Mg, Co, Ni, Zn, Al ferrite spinels: a multi-element approach EXAFS study. *Journal of Physics: Condensed Matter* **19**, 076214 (2007).

39. Rao, C. N. & Rao, K. K. Effect of Temperature on Lattice Parameters of Some Silver-Palladium Alloys. *Canadian Journal of Physics* **42**, 1336-1342 (1964).

40. Arenholz, E. & Prestemon, S. O. Design and performance of an eight-pole resistive magnet for soft X-ray magnetic dichroism measurements. *Reviews of Scientific Instruments* **76**, 083908/1-8 (2005).

41. van der Laan, G. & Thole, B. T. Strong magnetic X-ray dichroism in 2*p* absorption spectra of 3*d* transition metal ions. *Phys Rev B* **43**, 13401-13411 (1991).

42. Shirley, D. A. High-Resolution X-Ray Photoemission Spectrum of the Valence Bands of Gold. *Physical Review B* **5**, 4709-4714 (1972).

462 **Table Caption**

463

464 **Table 1.** Parameters obtained from fitting the Fe and Pd *K*-edges EXAFS spectra of
465 biomagnetite samples. *N* is the coordination number, r is the interatomic distance and $2\sigma^2$
466 is the Debye-Waller factor.

467

468 **Figure captions**

469

470 **Figure 1.** TEM images of, **a**, biomagnetite and, **b,** Pd-coated biomagnetite, inset contains
471 annotation indicating where EDX spectra were taken. **c**, selected area electron diffraction
472 (SAED) pattern for Pd-coated biomagnetite with reflections labelled in black (magnetite)
473 and grey (palladium) and, **d**, X-ray diffraction (XRD) of Pd-coated biomagetite.

474

475 **Figure 2.** TOF-SIMS images of (a) washed biogenic nanomagnetite produced by
476 *Geobacter sulfurreducens* and (b) commercially available inorganic nanomagnetite.
477 Normalised secondary ion ratio of the surface of washed biogenic magnetite before and
478 after ablation of the surface with a C_{60} gun.

479

480 **Figure 3. a,** EXAFS and, **b**, corresponding Fourier transform for the Fe K-edge of (i)
481 biomagnetite and (ii) Pd-coated bio-magnetite and Pd K-edge of (iii) Pd foil and (iv) Pd-
482 coated biomagnetite. Data (black lines) and fits (dotted red lines).

483

Figure 4. a, Fe $L_{2,3}$-edge XMCD spectra of (i), biomagnetite and (ii), Pd-coated biomagnetite and **b**, XPS of the Pd 3d peaks of biogenic Pd-coated magnetite

Figure 5. Rate of conversion during the Heck coupling of iodobenzene and ethyl acrylate catalysed by Pd-coated biomagnetite (solid lines) or Pd colloids (dashed lines). Fresh catalyst was used in run 1, runs 2 to 4 used recycled catalyst.

491 **Table 1**

492

	Atom type	*N*	r(Å)	$2\sigma^2$(Å^2)
		Fe *K*-edge		
Biomagnetite	O	1.3	1.85	0.039
	O	4	2.03	0.025
	Fe	4	3.00	0.021
	Fe	8	3.50	0.012
	O	4	3.36	0.027
Pd biomagnetite	O	1.3	1.80	0.037
	O	4	2.00	0.024
	Fe	4	2.99	0.024
	Fe	8	3.48	0.012
	O	4	3.28	0.009
		Pd *K*-edge		
Pd foil standard	Pd	12	2.74	0.012
	Pd	6	3.85	0.020
	Pd	24	4.77	0.020
	Pd	12	5.36	0.012
	Pd	24	6.14	0.029
Pd biomagnetite	Pd	12	2.74	0.014
	Pd	6	3.84	0.018
	Pd	24	4.79	0.030
	Pd	12	5.42	0.016
	Pd	24	6.08	0.030

493

494

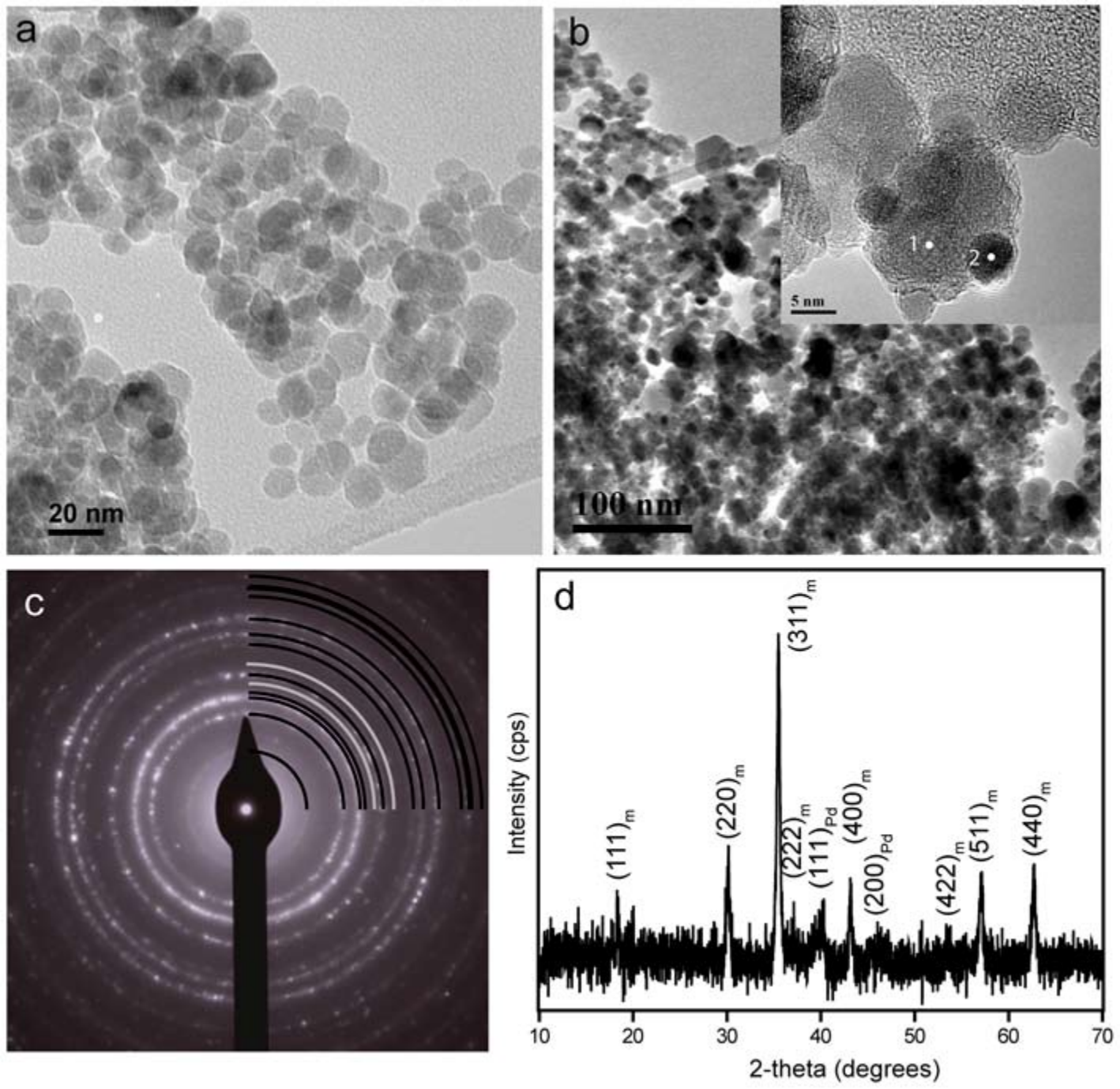
a
20 nm
b
100 nm
1
2
5 nm
c
d
Intensity (cps)
2-theta (degrees)
10
20
30
40
50
60
70
(111)m
(220)m
(311)m
(222)m
(111)Pd
(400)m
(200)Pd
(422)m
(511)m
(440)m

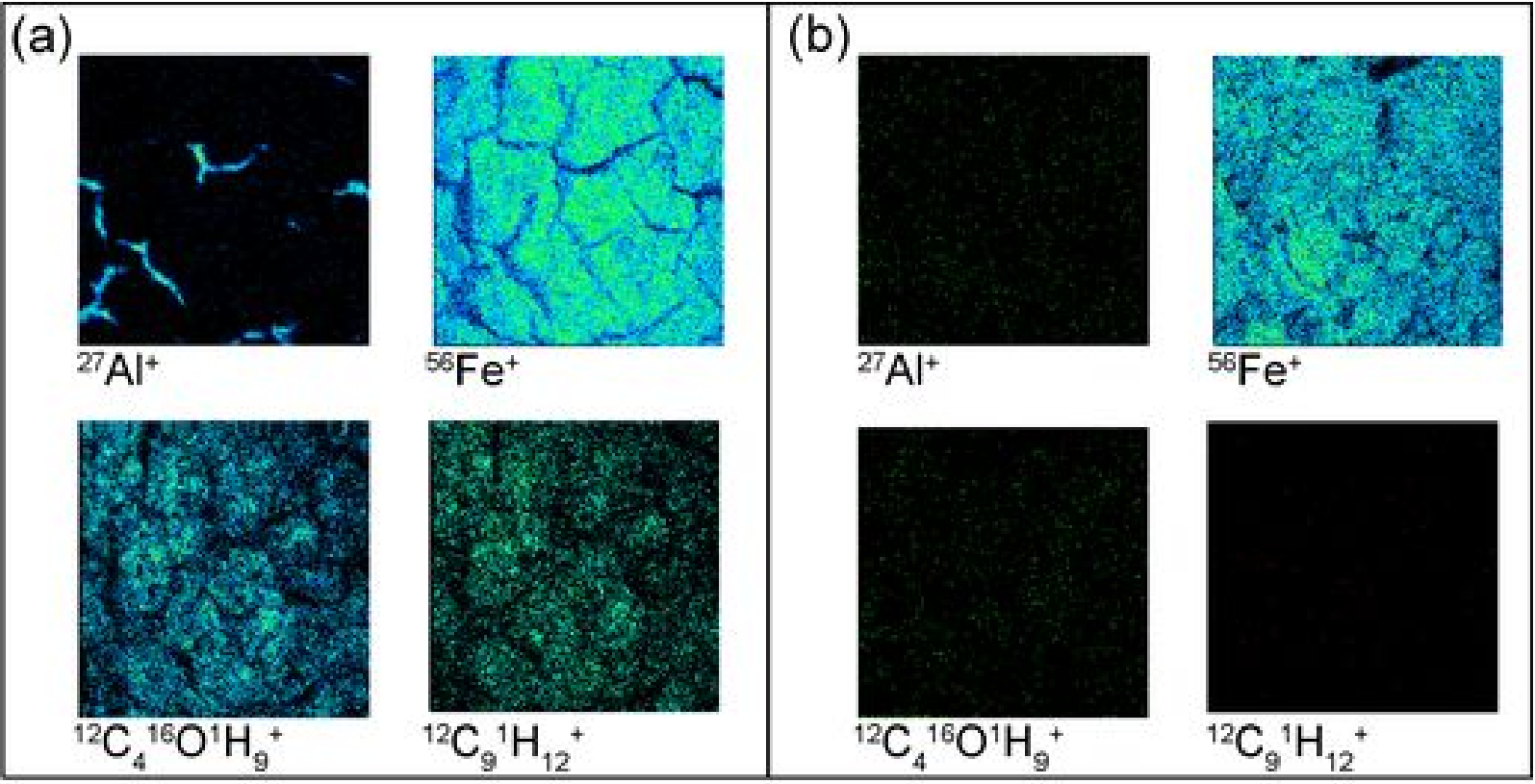
(a)
$^{27}Al^+$
$^{56}Fe^+$
$^{12}C_4{}^{16}O^1H_9{}^+$
$^{12}C_9{}^1H_{12}{}^+$
(b)
$^{27}Al^+$
$^{56}Fe^+$
$^{12}C_4{}^{16}O^1H_9{}^+$
$^{12}C_9{}^1H_{12}{}^+$

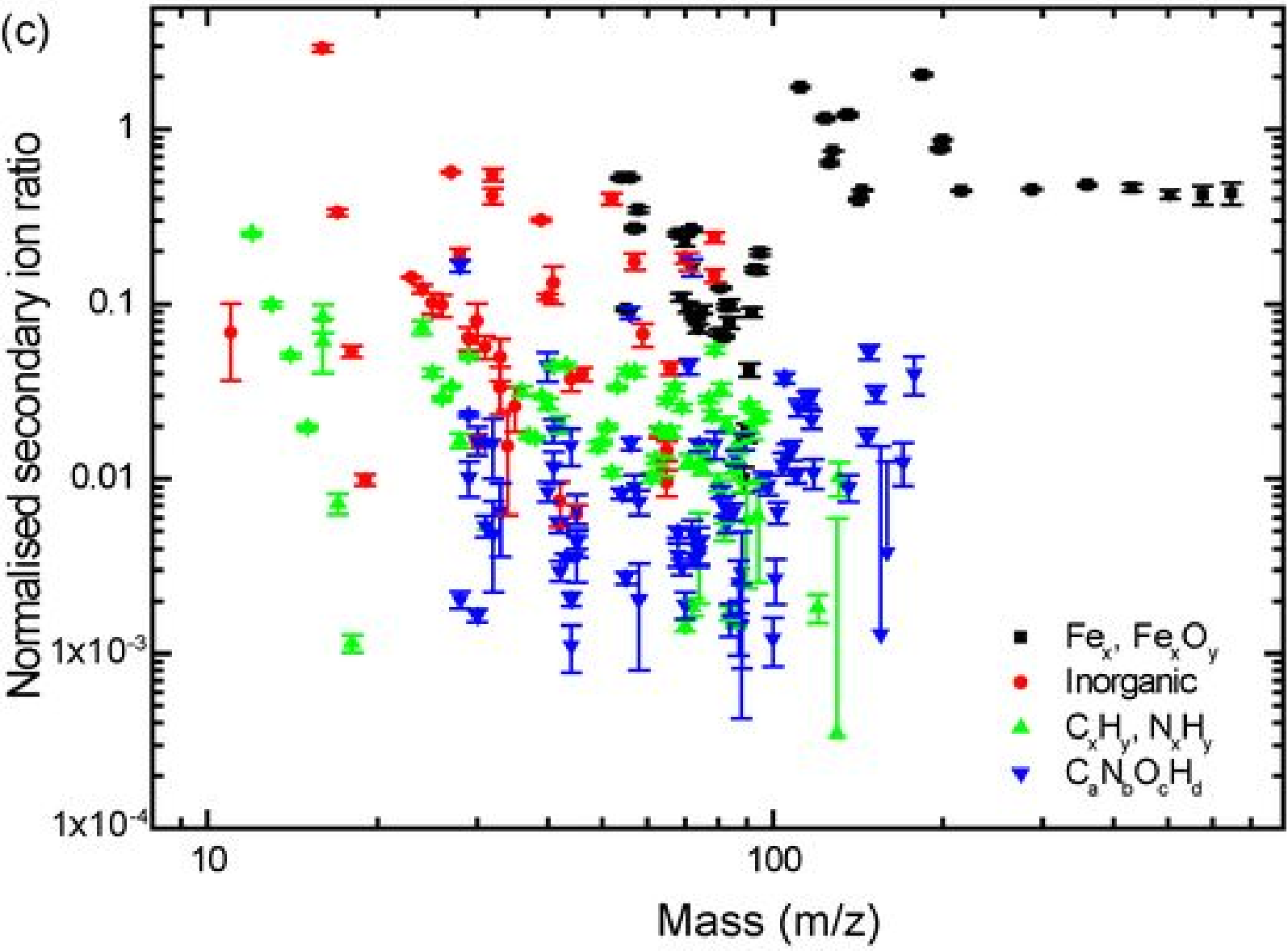
(c)
Normalised secondary ion ratio
1
0.1
0.01
1x10^{-3}
1x10^{-4}
10
100
Mass (m/z)
Fe_x, Fe_xO_y
Inorganic
C_xH_y, N_xH_y
$C_aN_bO_cH_d$

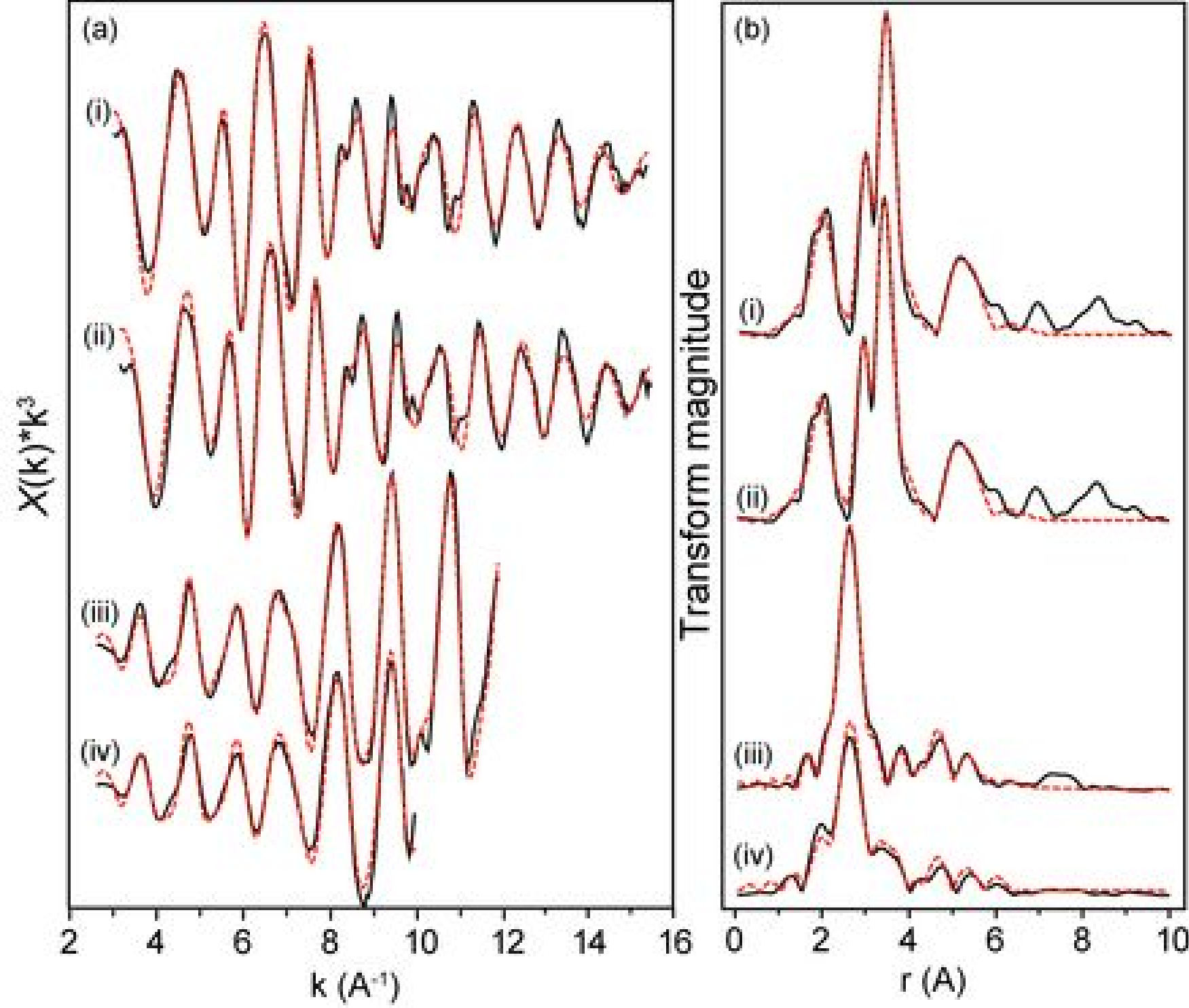
(a)
(i)
(ii)
(iii)
(iv)
χ(k)*k³
2
4
6
8
10
12
14
16
k (A⁻¹)
(b)
(i)
(ii)
(iii)
(iv)
Transform magnitude
0
2
4
6
8
10
r (A)

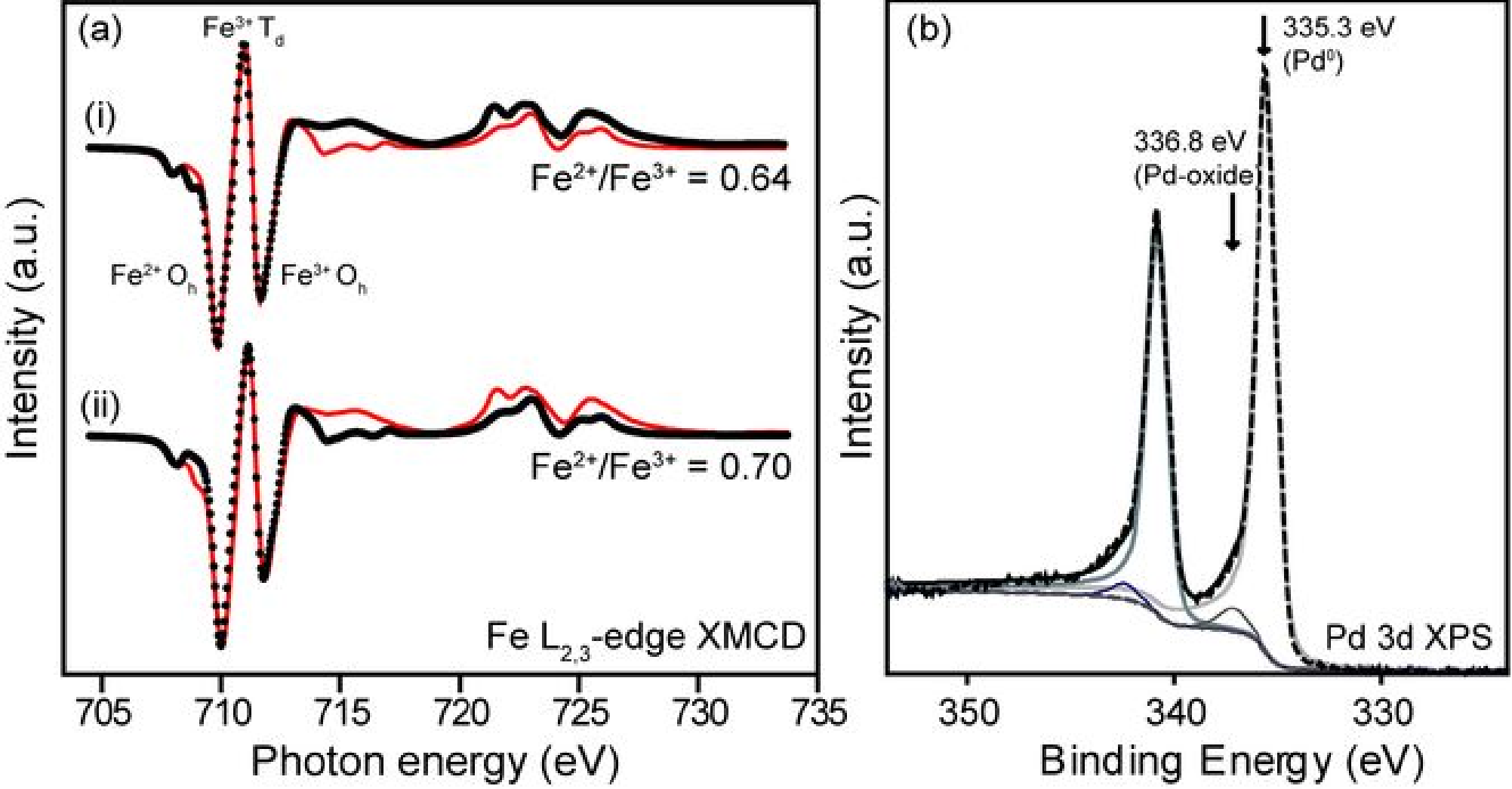
(a)
Fe3+ Td
(i)
Fe2+/Fe3+ = 0.64
Fe2+ Oh
Fe3+ Oh
(ii)
Fe2+/Fe3+ = 0.70
Fe L2,3-edge XMCD
Intensity (a.u.)
705
710
715
720
725
730
735
Photon energy (eV)
(b)
335.3 eV
(Pd0)
336.8 eV
(Pd-oxide)
Pd 3d XPS
Intensity (a.u.)
350
340
330
Binding Energy (eV)

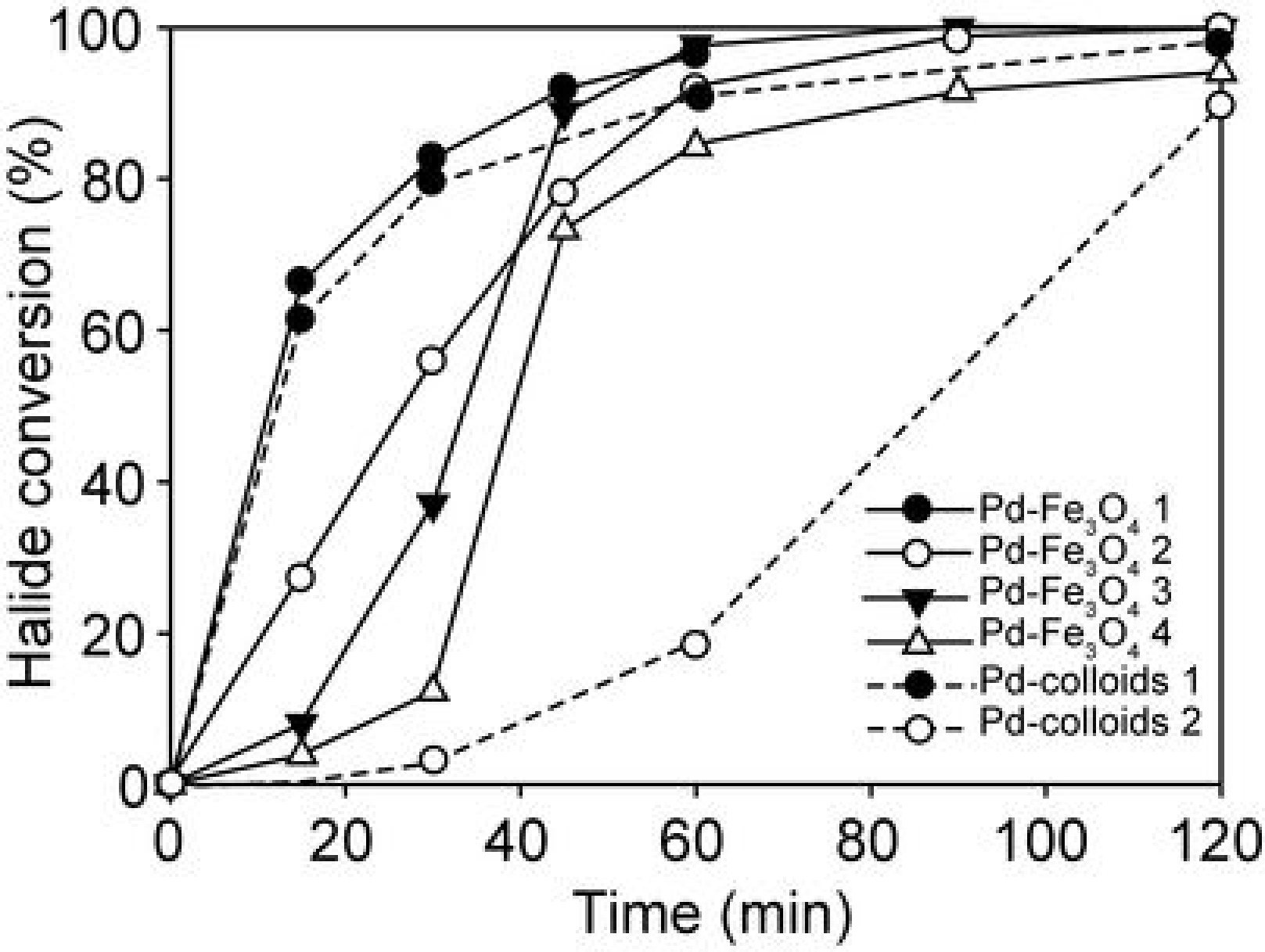
Halide conversion (%)
100
80
60
40
20
0
0
20
40
60
80
100
120
Time (min)
Pd-Fe3O4 1
Pd-Fe3O4 2
Pd-Fe3O4 3
Pd-Fe3O4 4
Pd-colloids 1
Pd-colloids 2